

Rb Doping and Lattice Strain Synergistically Engineering Oxygen Vacancies in TiO₂ for Stable High-Contrast Photoreversible Color Switching

Xiangyu Tian, Zixu Zeng, Yi He, Lecheng Lei, Chunlin Yu,* and Xingwang Zhang*

The utilization of TiO₂ for the fabrication of transparent photochromic materials is both cost-effective and environmentally friendly. However, it still poses challenges due to the rapid recombination of electron-hole pairs and poor organic-inorganic compatibility. Oxygen vacancies play a crucial role in sustaining sacrificial electron donors for hole scavenging, demonstrating great potential in enhancing photochromic performance. Herein, Rb doping and lattice strain are applied to synergistically engineer oxygen vacancies, considering lattice oxygen release is influenced by charge neutrality and oxygen atom coordination environment. Furthermore, the particle surface is modified using composite siloxanes to ensure monodispersion and enhance organic-inorganic compatibility. Structural analyses and theoretical calculations indicate that Rb doping and epitaxial strain synergistically reduce the oxygen vacancy formation energy and promote the chemical adsorption of diethylene glycol (DEG) on the TiO₂ surface for hole scavenging. The designed DEG-added Rb-TiO₂/TB-CS (TB means extra titanium butoxide, CS means composite siloxanes) nanodispersion exhibits a significant optical modulation amplitude exceeding 90% at 650 nm, rapid response within 60 s, and stable reversibility in color-switching (50 cycles). Moreover, utilizing Rb-TiO₂/TB-CS with DEG ligands as a responsive material enables the fabrication of transparent photochromic polyacrylate-based hybrid films, polyvinyl alcohol-based hydrogels, and hydroxyethyl cellulose-based rewritable papers, showcasing its immense potential for diverse applications.

pivotal role across various fields, including optical displays, sensors, and data storage.^[1] Furthermore, imparting transparency properties to these materials opens up new avenues for numerous applications such as smart windows, transparent displays, and wearable devices.^[2] However, the fabrication of transparent photochromic materials that demonstrate significant optical modulation amplitude, rapid response, and stable color-switching reversibility remains a challenge from both a technical and economic standpoint. Although organic photochromic molecules have undergone extensive development, the majority still necessitate intricate synthesis procedures and toxic precursors and exhibit unstable physicochemical properties.^[3] In contrast, photochromic transition metal oxides have higher thermal stability, chemical resistance, and strength.^[4] Titanium dioxide (TiO₂) is considered a promising functional component for photochromic materials due to its abundant elemental reserve, nontoxic nature, and physicochemical stability.^[5] In recent years, photochromic systems incorporating TiO₂ and redox dyes such as methylene blue (MB) have been developed to achieve reversible color switching through the reduction of

dyes by photogenerated electrons and oxidation of dyes by oxidant.^[6] However, such systems still suffer from low transparency, potential toxicity risks, and limited ability for reversible color-switching due to photocatalytic degradation of the dyes.

Constructing reversible photochromic systems in which TiO₂ itself functions as the color-changing component is anticipated to address the aforementioned issues. To achieve high transparency of the composite materials, it is necessary for the particle size of TiO₂ to be less than 40 nm (one-tenth of the minimum wavelength of visible light).^[7] Additionally, a sufficiently elevated concentration of TiO₂ within the polymer matrix is required to ensure large optical modulation amplitude (high contrast).^[8] Therefore, surface modification becomes imperative to guarantee particle monodispersity and enhance organic-inorganic compatibility for the prevention of Rayleigh scattering. In these systems, the redox between Ti(IV) and Ti(III) driven by photoinduced electrons and oxygen enables reversible color switching between white and

1. Introduction

The utilization of photochromic materials capable of reversible color switching in response to external light stimuli has played a

X. Tian, Z. Zeng, Y. He, L. Lei, C. Yu, X. Zhang
 Key Laboratory of Biomass Chemical Engineering of Ministry of Education
 Department of Chemical and Biological Engineering
 Zhejiang University
 Hangzhou 310027, China
 E-mail: chunlinyu@zju.edu.cn; xwzhang@zju.edu.cn
 C. Yu
 Institute of Zhejiang University-Qzhou
 Qzhou 324000, China

 The ORCID identification number(s) for the author(s) of this article can be found under <https://doi.org/10.1002/adfm.202423514>

DOI: 10.1002/adfm.202423514

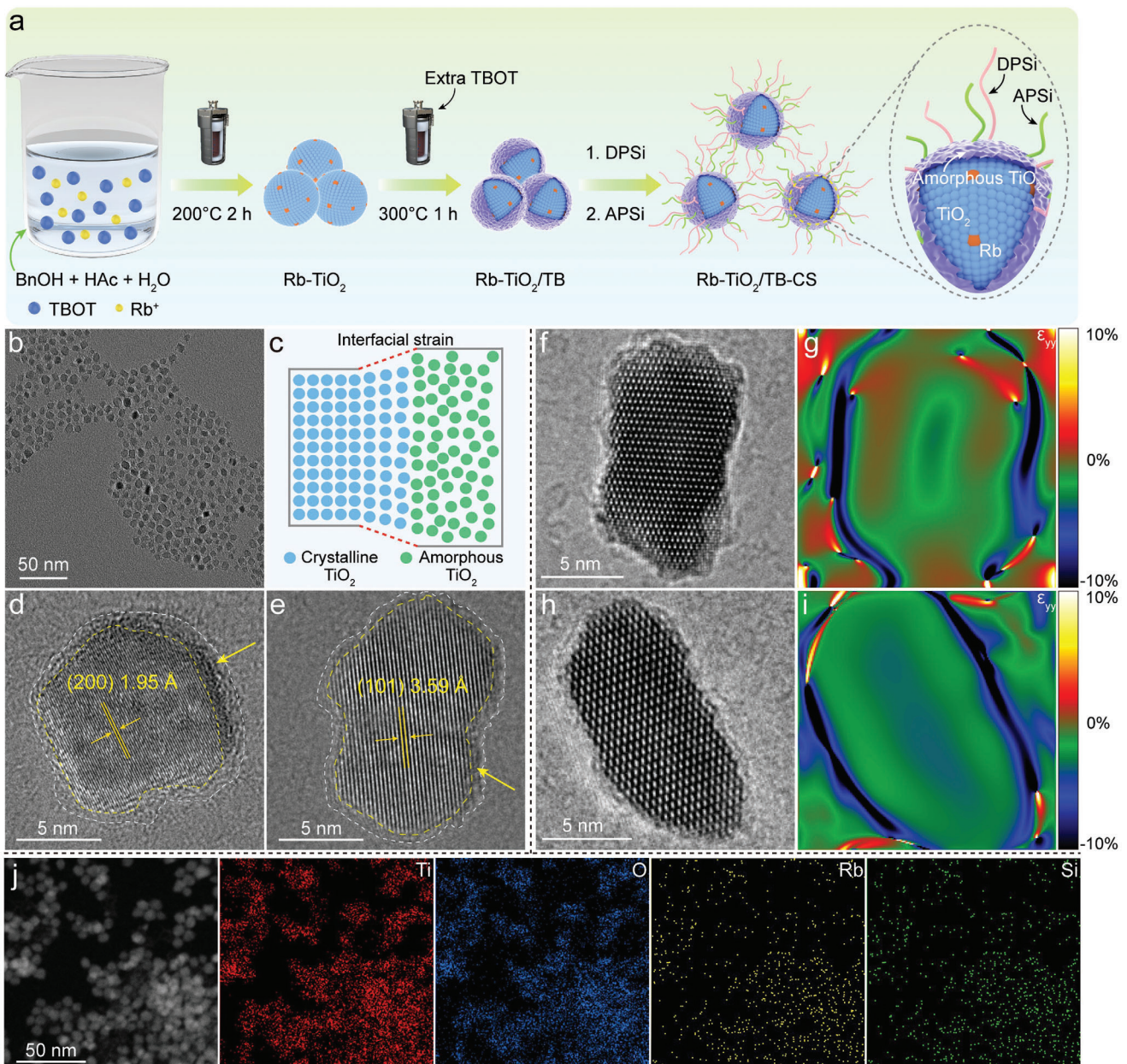


Figure 1. a) Schematic diagram for the fabrication of Rb-TiO₂/TB-CS nanoparticles. b) TEM image for Rb-TiO₂/TB-CS. c) Schematic illustration of epitaxial strain at the crystalline-amorphous interface. d) and e) High-resolution TEM images for Rb-TiO₂/TB-CS (The areas indicated by the yellow arrows are the amorphous structures). f) High-resolution TEM image and g) corresponding strain mapping from GPA of TiO₂/TB. h) High-resolution TEM image and i) corresponding strain mapping from GPA of Rb-TiO₂/TB. j) Elemental maps for Rb-TiO₂/TB-CS.

dark blue. Fundamentally, the performance of photochromism, including response speed and optical modulation amplitude, critically relies on the efficient scavenging of photoinduced holes, which allows photoinduced electrons to escape recombination and reduce Ti(IV).

Notably, oxygen vacancies with localized electrons play a key role in hole scavenging. On one hand, it has been reported that oxygen vacancies directly act as sacrificial electron donors (SEDs) to capture photoinduced holes.^[9] On the other hand, oxygen vacancies can serve as reaction sites for the dissociation of

organic adsorbates. Chemisorbed alcohol ligands on TiO₂ surfaces have been proven to function as SEDs to scavenge holes.^[10] Thus, the photochromic performance can be substantially enhanced through oxygen vacancies engineering, while ensuring the preservation of surface groups crucial for subsequent modification and application. To modulate the electronic structure for facilitating the generation of oxygen vacancies, it is preferable to introduce low-valent metal ions as dopants into TiO₂ in order to reduce the energy required for oxygen vacancy formation, which is induced by the retention of charge neutrality.^[11] Furthermore,

the formation of oxygen vacancies, which is influenced by the coordination environment of the oxygen atoms, is associated with lattice expansion resulting from electron localization on neighboring cations.^[12] Lattice strain has been demonstrated to distort local bonding and impact the ligand field.^[13] Additionally, tensile strain is considered to decrease the migration barrier for oxygen atom transfer and surface exchange, indicating a strong correlation between lattice strain and oxygen defect chemistry.^[14] Therefore, doping low-valent metal ions and engineering lattice strain may synergistically reduce the oxygen vacancy formation energy, thereby promoting the abundant generation of oxygen vacancies in TiO₂.

Herein, we present a novel Rb-TiO₂/TB-CS photochromic responsive structure for the construction of reversible photochromic systems. The synergistic strategy of rubidium (Rb) doping and lattice strain greatly facilitates the generation of oxygen vacancies and enhances the chemical adsorption of DEG molecules on the TiO₂ surface, which efficiently acts as SEDs to scavenge holes. Additionally, surface modification using composite siloxanes ensures the monodispersion of nanoparticles and improves organic-inorganic compatibility. The Rb-TiO₂/TB-CS nanodispersion, with the addition of DEG, exhibits high transparency and can undergo rapid coloration from clear to dark blue in tens of seconds under UV irradiation. Moreover, it conveniently fades through air oxidation. Notably, this nanodispersion demonstrates an ultrahigh optical modulation amplitude exceeding 90% at 650 nm and enhanced color-switching reversibility (50 cycles) compared to previous studies. The polyacrylate-based transparent photochromic hybrid film, fabricated with Rb-TiO₂/TB-CS and possessing excellent flexibility, exhibits a high optical contrast of 82.74% at 650 nm in photochromic process and can be photo-printed with complex patterns and texts in high resolution. Additionally, by utilizing Rb-TiO₂/TB-CS with DEG ligands, polyvinyl alcohol (PVA)-based transparent photochromic hydrogels and hydroxyethyl cellulose (HEC)-based rewritable papers can also be prepared. In summary, compared with published work, the Rb-TiO₂/TB-CS as an exceptional photochromic structure possesses high transparency, superior optical modulation amplitude, enhanced color-switching reversibility, and adaptability to various systems, enabling diverse applications such as photochromic windows, transparent displays, wearable devices, and temporary data storage.

2. Result and Discussion

2.1. Preparation and Characterization of Rb-TiO₂/TB-CS Structure

The fabrication of the Rb-TiO₂/TB-CS structure is schematically illustrated in Figure 1a. The Rb-doped TiO₂ was prepared by the first solvothermal process. Subsequently, the crystalline-amorphous interface was constructed to induce lattice strain during the second solvothermal process with the extra addition of titanium butoxide (TBOT). Surface modification was performed using composite siloxanes of 3,3-dimethoxy-2,7,10,13,16-pentaoxa-3-silaheptadecane (DPSi) and 3-(acryloyloxy)propyltrimethoxysilane (APSi) to enable monodispersity of the nanoparticles (NPs) in polar solvents and provide cross-linking sites for hybridization, respectively. Pre-experiments were used to optimize the structure and guide the

following investigations. The microscopic state of modified Rb-TiO₂-CS with various feeding molar ratios of Rb/Ti (2%, 5%, 10%, and 20%) was presented in Figure S1 (Supporting Information). With increasing Rb doping levels, Rb-TiO₂-CS NPs gradually grow and agglomerate. The heteroatoms are more inclined to be enriched in the shallow surface region of the particles.^[15] As the dopant concentration increases, defects and heteroatom sites accommodated in TiO₂ crystals become saturated, causing rubidium oxides to precipitate on the TiO₂ surface, leading to the aggregation of neighboring particles through bridging interactions (Figure S2, Supporting Information).^[16] Based on the above results, the feeding ratio of Rb/Ti is determined to be 5%. It should be mentioned that Rb-TiO₂-CS exhibits an unstable dispersion after 24 h (Figure S3, Supporting Information), which makes it unsuitable for comparison in further characterizations and performance tests. The morphology of TiO₂/TB-CS with different TBOT additions in the second solvothermal process was also investigated (Figure S4, Supporting Information). As the amount of the second addition of TBOT increases, the particles crosslink with each other through amorphous structure and the boundaries become blurred, so the amount of second TBOT addition is determined to be 20% of the first TBOT addition. The sample prepared according to the optimal conditions of the pre-experiments is denoted as Rb-TiO₂/TB-CS. The transmission electron microscopy (TEM) image shown in Figure 1b displays the monodispersion and narrow size distribution of the Rb-TiO₂/TB-CS NPs. Compared to agglomerated Rb-TiO₂/TB NPs without modification (Figure S5a, Supporting Information), the Rb-TiO₂/TB-CS NPs are uniformly monodispersed and exhibit an average particle size of 10.5 nm (Figure S5b,c, Supporting Information).

Figure 1c illustrates the epitaxial strain at the crystalline-amorphous interface mediated by the uneven volumetric shrinkage during the solvothermal process.^[17] The high-resolution TEM images of Rb-TiO₂/TB-CS shown in Figure 1d,e demonstrate the construction of the crystalline-amorphous interface, which is formed through the in situ growth of amorphous structure on the well-crystallized Rb-TiO₂. For Rb-TiO₂/TB-CS, the lattice spacing of 1.95 Å corresponds to the (200) plane, and the lattice spacing of 3.59 Å belongs to the (101) plane.^[18] Compared to the lattice spacing of 1.90 Å (200) and 3.51 Å (101) for pure TiO₂ (Figure S6, Supporting Information), the increased lattice spacing of Rb-TiO₂/TB-CS indicates the successful doping of Rb, and the increased lattice spacing of Rb-TiO₂ displayed in Figure S7 (Supporting Information) also supports it. To avoid the interference of surface modifiers on the interfacial lattice strain, the unmodified TiO₂/TB and Rb-TiO₂/TB are characterized by high-resolution TEM in Figure 1f,h, respectively, in which the crystalline-amorphous interfaces both are clearly visible. Geometric phase analysis (GPA) is a widely used technique that relies on the spatial transformation of crystal phases for the analysis of TEM images. GPA is based on electron diffraction theory for phase deconvolution, which is effective for investigating local lattice strains, distortions, and defects.^[19] To quantitatively investigate the distribution of strain, GPA is performed to analyze the high-resolution TEM images of unmodified TiO₂/TB and Rb-TiO₂/TB. The results of GPA in Figure 1g,i both demonstrate that the clear axial tensile strain (ϵ_{yy}) is distributed along the crystalline-amorphous interfaces in TiO₂/TB and Rb-TiO₂/TB, which should be caused by the difference of

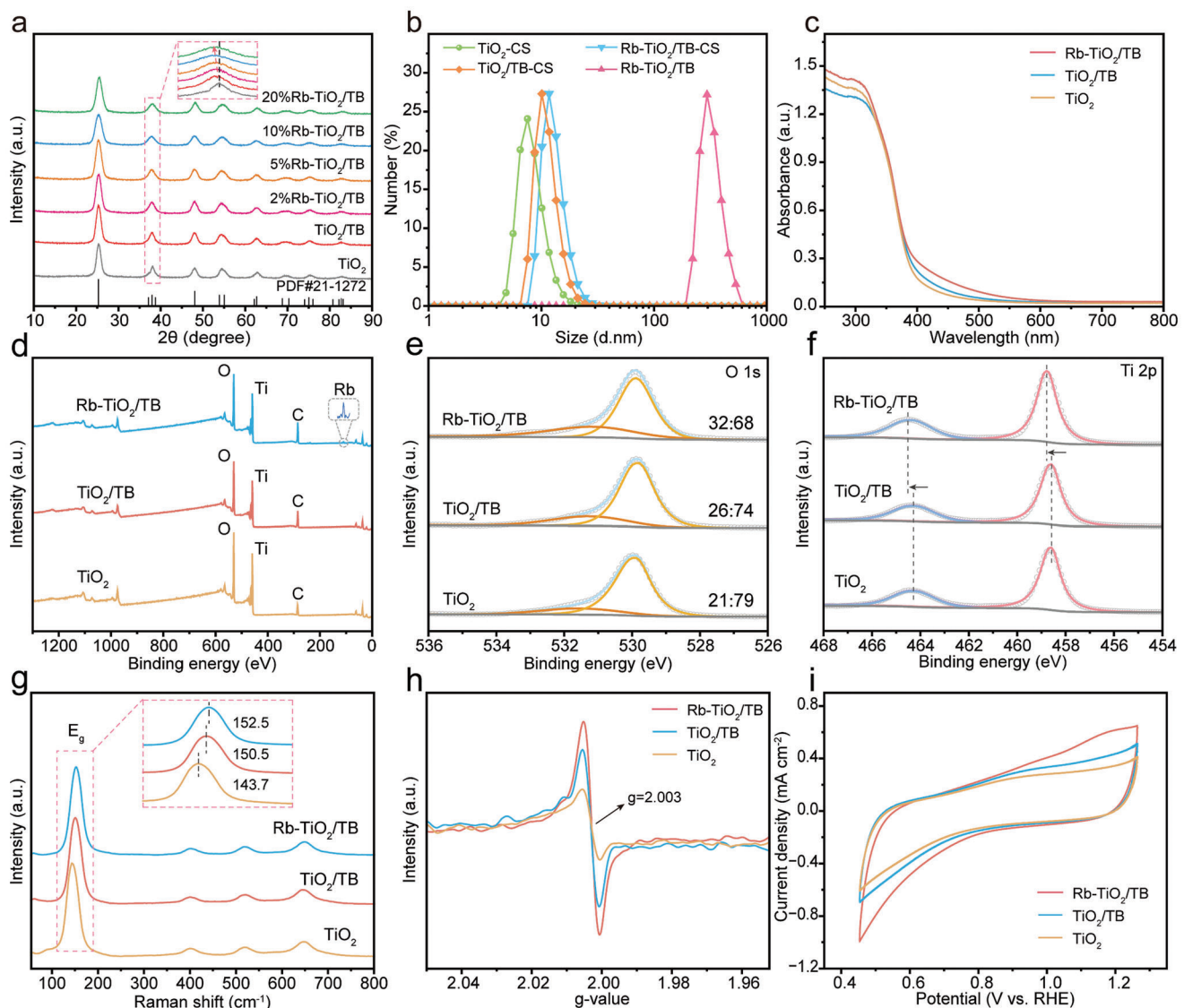


Figure 2. a) XRD patterns of TiO_2 and TiO_2/TB with various Rb/Ti feeding molar ratios. b) The number distribution of particle size for $\text{TiO}_2\text{-CS}$, $\text{TiO}_2\text{/TB-CS}$, $\text{Rb-TiO}_2\text{/TB-CS}$, and unmodified $\text{Rb-TiO}_2\text{/TB}$ in PGMEA. c) UV-vis diffuse reflectance spectra, d) Survey XPS spectra, e) XPS spectra of O 1s, f) XPS spectra of Ti 2p, g) Raman spectra, h) EPR spectra without light irradiation, and i) CV curves for TiO_2 , TiO_2/TB , and $\text{Rb-TiO}_2/\text{TB}$.

volumetric shrinkage between crystalline and amorphous solid. Furthermore, the homogeneous distributions of Ti, O, Rb, and Si elements in $\text{Rb-TiO}_2/\text{TB-CS}$ are confirmed by the elemental mappings in Figure 1j. The practical Rb/Ti ratios in $\text{Rb-TiO}_2/\text{TB-CS}$ measured by the energy-dispersive spectrometer (EDS) and inductively coupled plasma optical emission spectrometry (ICP-OES) both are close to 2% (Figure S8 and Table S1, Supporting Information). However, this is different from the feeding ratio of 5%, which may be explained by the fact that only part of the Rb^+ ions are successfully doped into TiO_2 due to the large radius of Rb^+ ions. Moreover, from the elemental maps for $\text{Rb-TiO}_2/\text{TB-CS}$ with a higher Rb/Ti feeding ratio of 10% shown in Figure S9 (Supporting Information), it can be seen that the Rb element is uniformly distributed without significant aggregation, indicating that Rb can be uniformly doped

during the synthesis rather than tending to generate rubidium oxides.

To further investigate the crystalline structure, the X-ray diffraction (XRD) patterns are presented in Figure 2a. All diffraction peaks of samples correspond to those of the anatase TiO_2 phase according to JCPDS No. 21–1272. It is noteworthy that the diffraction peak of the (004) plane shifts negatively as the Rb/Ti feeding ratio increases, which indicates that Rb^+ ions with a larger ionic radius are successfully doped into the lattice of TiO_2 . The size distributions of nanodispersions reflect the actual state of the NPs. Figure 2b displays the number distribution of particle size for $\text{TiO}_2\text{-CS}$, $\text{TiO}_2\text{/TB-CS}$, $\text{Rb-TiO}_2\text{/TB-CS}$, and unmodified $\text{Rb-TiO}_2\text{/TB}$ in propylene glycol monomethyl ether acetate (PGMEA). Compared to unmodified $\text{Rb-TiO}_2\text{/TB}$ with an average size of 295 nm, the $\text{Rb-TiO}_2\text{/TB-CS}$ exhibits an

average size of 11.7 nm, which is roughly consistent with the statistics of the TEM, suggesting the monodispersion of Rb-TiO₂/TB-CS NPs in PGMEA. In addition, although the particle size of Rb-TiO₂/TB-CS is slightly increased in comparison to TiO₂-CS and TiO₂/TB-CS, it is sufficiently smaller than 40 nm to prevent Rayleigh scattering of visible light. Furthermore, the light absorption of samples in unexcited states directly affects the transparency and photochromic contrast of the hybrid materials. The UV-vis diffuse reflectance spectra (DRS) shown in Figure 2c indicate that the Rb-TiO₂/TB shows almost no absorption in the 600–800 nm region and exhibits a slightly increasing absorption in the 400–600 nm region in contrast to TiO₂ and TiO₂/TB, which may be due to the precipitation of rubidium oxides on the surface.

The X-ray photoelectron spectroscopy (XPS) was utilized to explore the chemical environment and electronic interactions of Rb-TiO₂/TB. All binding energy signals were calibrated with the C 1s peak at 284.8 eV. The survey XPS spectra shown in Figure 2d demonstrate the existence of Ti, Rb, O, and C elements in Rb-TiO₂/TB. The Rb 3D spectrum of Rb-TiO₂/TB shown in Figure S10 (Supporting Information) confirms the Rb⁺ chemical state.^[20] In the high-resolution O 1s spectra (Figure 2e), the peak at 529.81 eV is attributed to the lattice oxygen, and the peak at 531.26 eV is assigned to the surface -OH groups.^[21] Moreover, the higher binding energy peak of O 1s can be directly related to oxygen vacancies or surface defects.^[22] Based on the changing trend of the peak area at 531.26 eV, it can be inferred that lattice strain and Rb doping facilitate the formation of more oxygen vacancies, providing Rb-TiO₂/TB with the most oxygen defects. Figure 2f presents the high-resolution Ti 2p spectra. For TiO₂ and TiO₂/TB, the peaks at 458.59 and 464.26 eV are attributed to Ti 2p_{3/2} and Ti 2p_{1/2}, respectively.^[23] Intriguingly, the binding energies of Ti 2p_{3/2} and Ti 2p_{1/2} for Rb-TiO₂/TB shift positively by 0.17 and 0.11 eV, respectively. This may be explained that Rb only provides one valence electron and the strong electronegativity of O still contributes to maintaining the electron density on O, which further reduces the electron density on Ti, confirming the modulation of Rb doping on the electronic structure.

To further understand the structure of Rb-TiO₂/TB, the Raman spectroscopy study was carried out. As shown in Figure 2g, all Raman spectra show the characteristic Raman bands of the anatase TiO₂ phase with the strongest E_g band.^[24] The E_g band of TiO₂/TB (150.5 cm⁻¹) exhibits a shift toward higher wavenumbers compared to that of pure TiO₂ (143.7 cm⁻¹), and the E_g band of Rb-TiO₂/TB is further shifted to 152.5 cm⁻¹. According to previous studies, the blue shift of the Raman peak is characteristic of non-stoichiometric TiO₂ and represents the disruption of lattice periodicity and octahedral symmetry, which is directly related to surface oxygen defects.^[25] This may indicate that tensile strain promotes the formation of oxygen vacancies, which is further facilitated by Rb doping through synergistic effects. The electron paramagnetic resonance (EPR) spectra used to further elucidate the presence of oxygen vacancies are displayed in Figure 2h. It is known that the EPR signal at g = 2.003 is attributed to electron-trapped oxygen vacancies.^[26] Rb-TiO₂/TB exhibits the strongest EPR signal followed by TiO₂/TB, and TiO₂ shows the weakest EPR signal, which is consistent with the ordering of their oxygen vacancy abundances. The cyclic voltammetry (CV) measurement was also performed to visually compare the concentration of oxy-

gen vacancies. As shown in Figure 2i and Figure S11 (Supporting Information), the larger oxidation peak area indicates a greater number of oxygen vacancies.^[27] In agreement with the results of Raman and EPR characterizations, the oxygen vacancies concentration is ranked as: Rb-TiO₂/TB > TiO₂/TB > TiO₂. The above results corroborate with each other, strongly demonstrating the synergistic promotion by tensile strain and Rb doping for the formation of oxygen vacancies.

2.2. Photochromism Performance Evaluation

Previous studies have revealed two mechanisms of oxygen vacancies in hole scavenging oxygen vacancies possessing localized electrons that may directly serve as SEDs, and alcohols dissociatively adsorbed at oxygen vacancy sites on the surface can also act as SEDs.^[6b,d,9] However, when we subjected the Rb-TiO₂/TB-CS PGMEA nanodispersions with and without the addition of DEG under UV irradiation, DEG-added nanodispersion showed a much more intense dark blue color than the DEG-unadded nanodispersions (Figure S12, Supporting Information). This suggests that chemisorbed DEG is more effective in scavenging holes than oxygen vacancies themselves. Additionally, compared to other polyols, DEG exhibits a stronger hole scavenging ability and stability, thereby making it the sacrificial electron donor in our system (Figure S13, Supporting Information). Furthermore, the number of oxygen defect sites has been reported to directly affect the number of surface chemisorbed alcohols.^[28] To confirm this idea, the FT-IR spectra of samples, which were initially unmodified and were submerged in DEG under UV irradiation followed by multiple washes and centrifugation, are shown in Figure 3a. It can be seen that the abundance of oxygen vacancies in samples is positively correlated with the intensity of the peaks assigned to DEG, suggesting that oxygen vacancies act as reaction sites to promote the dissociative adsorption of DEG. In addition, compared to unmodified Rb-TiO₂/TB, peaks of the corresponding modifiers (APSi and DPSi) appear on the spectrum of Rb-TiO₂/TB-CS, indicating successful surface modification.

The DEG-added Rb-TiO₂/TB-CS nanodispersion (volume ratio, PGMEA:DEG = 4:1) before and after UV irradiation was subjected to EPR analysis (Figure 3b). It can be seen that a clear signal appears at g = 1.941 after UV irradiation, which is attributed to Ti³⁺.^[27c] This confirms that the Ti⁴⁺ is reduced to Ti³⁺ by photogenerated electrons after the scavenging of holes during the photochromism process. In addition, there is still a signal of oxygen vacancies appearing after UV irradiation, which further suggests that oxygen vacancies are difficult to act as SEDs directly. To further understand the coloration mechanism of photochromism, Figure 3c shows the optical absorption of DEG-added Rb-TiO₂/TB-CS nanodispersion before and after UV irradiation. The DEG-added Rb-TiO₂/TB-CS nanodispersion without UV irradiation almost shows no absorption in visible and near-infrared regions, exhibiting excellent transparency. Notably, the DEG-added Rb-TiO₂/TB-CS nanodispersion after UV irradiation exhibits a distinct dark blue color and shows increased optical absorption from visible to near-infrared region. The absorption in the visible region is attributed to the formation of Ti³⁺ by the reduction of photogenerated electrons, while most of the photogenerated electrons remain as free carriers which may

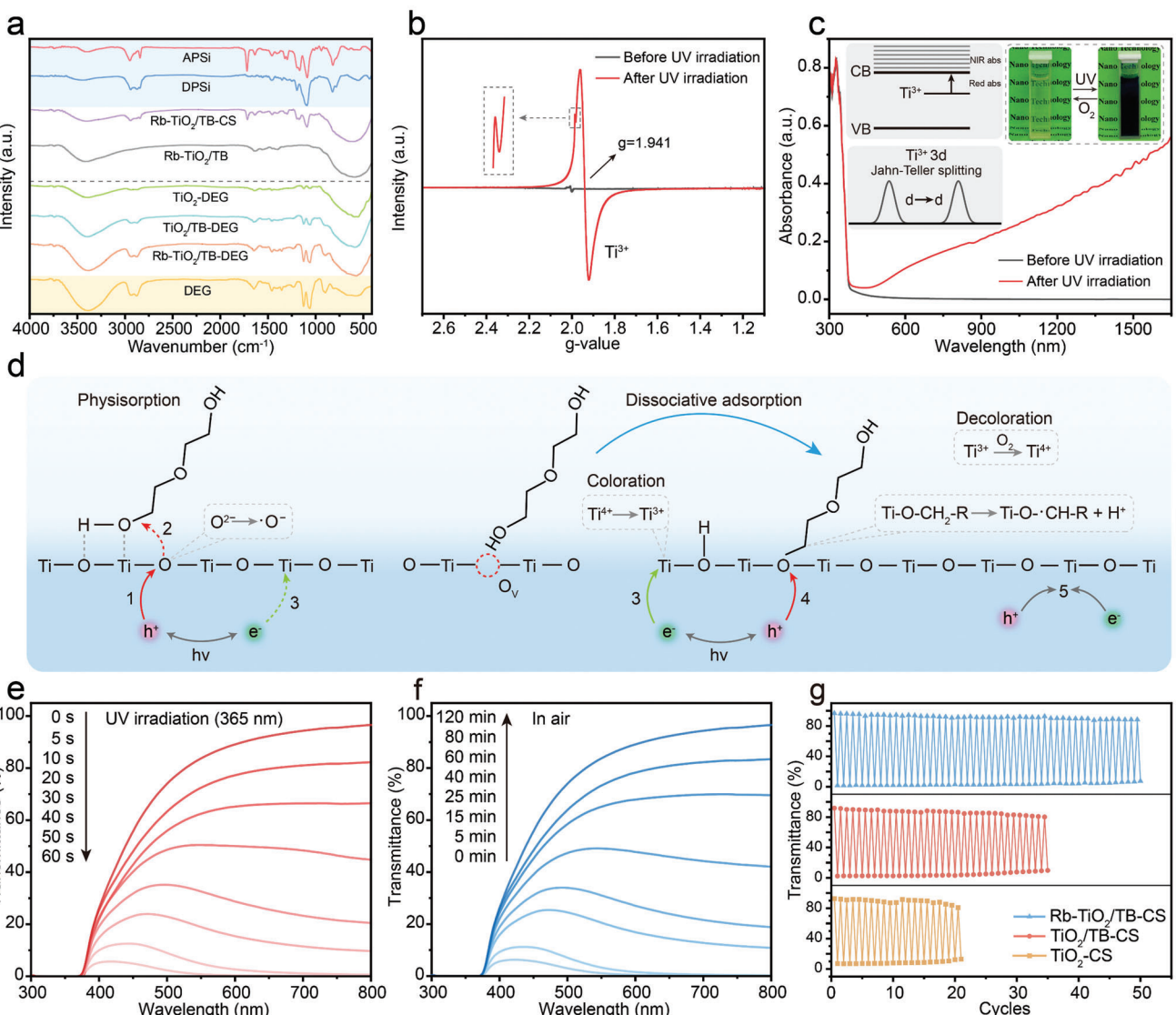


Figure 3. a) FT-IR spectra for Rb-TiO₂/TB, modified Rb-TiO₂/TB-CS, TiO₂-DEG, TiO₂/TB-DEG, and Rb-TiO₂/TB-DEG. b) EPR spectra for DEG-added Rb-TiO₂/TB-CS nanodispersion (volume ratio, PGMEA:DEG = 4:1) before and after UV irradiation. c) Optical absorption of DEG-added Rb-TiO₂/TB-CS nanodispersion before and after UV irradiation, the inset shows the optical image of this nanodispersion and the color development mechanism of Ti³⁺. d) The schematic illustration of the color-switching mechanism of DEG-added Rb-TiO₂/TB-CS nanodispersion. e) UV-vis transmission spectra of DEG-added Rb-TiO₂/TB-CS nanodispersion during UV irradiation. f) UV-vis transmission spectra of colored DEG-added Rb-TiO₂/TB-CS nanodispersion in air. g) The plots of the transmittance at 650 nm of DEG-added TiO₂-CS, TiO₂/TB-CS, and Rb-TiO₂/TB-CS nanodispersions in cyclic tests for photochromism and discoloration.

cause localized surface plasmon resonance (LSPR) leading to the absorption in the near-infrared region.^[29] As shown in the inset of Figure 3b, there are two explanations for the coloration caused by Ti³⁺. On the one hand, Ti³⁺ introduces intermediate energy levels in the bandgap of TiO₂, leading to the absorption of visible and partial near-infrared light. On the other hand, density functional theory (DFT) calculations combined with two-photon photoemission spectroscopy (2PPE) have revealed that the 3D orbitals of Ti³⁺ are split into a wide occupied band gap state and an empty excited state by Jahn-Teller induced splitting.^[30] The d-d transitions from the wide occupied state to the excited state enhance the absorption in the visible region. Therefore, the ex-

tended visible absorption and near-infrared absorption together result in an absorption minimum in the blue region, which explains the dark blue color of the samples.

Figure 3d displays the schematic illustration of the color-switching mechanism of DEG-added Rb-TiO₂/TB-CS nanodispersion. Electrons and holes are produced by UV excitation. For physisorbed DEG on the particle surface, hole scavenging involves two processes: the trapping of the hole (step 1, \approx fs) and the abstraction of hydrogen from physisorbed DEG (step 2, \approx ns).^[31] The hole is first trapped by the lattice oxygen to form the Ti⁴⁺-•O⁻ radical, while the abstraction of hydrogen from DEG by that radical is too slow to compete with the recombination of

electron-hole pairs (step 5, \approx ps). Hence, the physisorbed DEG can hardly serve as an effective SED to scavenge holes. For dissociatively adsorbed DEG, the hole can be directly trapped in a 2p orbital by the bridging oxygen (step 4, \approx fs), and a fast deprotonation process is performed to form a relatively stable ketyl radical $\text{Ti}^{4+}\text{-O}\cdot\text{CH-R}$.^[32] Due to the faster hole scavenging than recombination of carriers, the electron can be localized on Ti^{4+} to form Ti^{3+} (step 3), allowing for the coloration of photochromism. The decoloration is carried out by the oxidation of O_2 . Detailed mechanistic equations are presented in supporting information. The color-switching performance and reversible stability of DEG-added $\text{Rb-TiO}_2/\text{TB-CS}$ nanodispersion are further investigated. The mass fraction of $\text{Rb-TiO}_2/\text{TB-CS}$ in the nanodispersion (volume ratio, PGMEA:DEG = 4:1) is 9.2%. As shown in Figure 3e, the transmittance of the nanodispersion gradually decreases with the increasing time of UV irradiation and reaches the minimum in 60 s, indicating the rapid response of this photochromism system. Notably, a large optical modulation amplitude is displayed, which is as high as 91.54% at 650 nm. The photochromism performance of the nanodispersion under sunlight is also investigated. The relevant data and experiment details are shown in Figure S14 (Supporting Information). The transmittance of the nanodispersion decreases with the increasing sunlight exposure time and gradually approaches the minimum after 150 min. The optical modulation amplitude is measured to be 79.5% at 650 nm, and the nanodispersion still can present clear photochromic color switching (Figure S15, Supporting Information). Figure 3f shows the transmittance of this system during the decoloration process in air. The transmittance of colored nanodispersion increases with the gradual oxidation of Ti^{3+} by oxygen and recovers to its initial state after 120 min. The physical adsorption layer of DEG on the particle surface may stabilize the coloring state by blocking O_2 . In addition, rapid decoloration in seconds can be achieved by injecting air directly into the nanodispersion repeatedly (Video S1, Supplementary Video1).

The color-switching reversibility of three samples is compared in Figure 3g. The initial response time is used as the UV irradiation time in color-switching cycle tests. DEG-added TiO_2/CS and $\text{TiO}_2/\text{TB-CS}$ nanodispersions exhibit optical modulation amplitudes less than 70% after 21 and 35 color-switching cycles, respectively. The hole scavenging rate is positively correlated with the number of DEG chemisorbed on the particle surface. It can be found that the initial optical modulation amplitude of $\text{Rb-TiO}_2/\text{TB-CS}$ is higher than others in the same irradiation time. Furthermore, the abundant oxygen vacancies of $\text{Rb-TiO}_2/\text{TB-CS}$ enable the nanodispersion stable color-switching reversibility, whose optical modulation amplitude is still more than 80% after 50 cycles. These results demonstrate oxygen vacancies engineering significantly enhances the photochromic performance including optical modulation amplitude, response speed, and color-switching reversibility. The reduction in photochromic performance after multiple cycles may be caused by the inactivation of a minor part of oxygen vacancies. The inactivation of oxygen vacancies is attributed to the adsorption and dissociation of O_2 and the dissociative adsorption of H_2O to form surface hydroxyl groups.^[33] The EPR spectra of DEG-added $\text{Rb-TiO}_2/\text{TB-CS}$ nanodispersion before and after 50 color-switching cycles in Figure S16 (Supporting Information) display that the intensity of the signal belonged to oxygen vacancy is slightly decreased after

50 cycles, demonstrating the consumption of oxygen vacancies in photoreversible color-switching process.

Furthermore, to study the long-term stable color-switching performance of $\text{Rb-TiO}_2/\text{TB-CS}$, the changes in morphology and surface structure before and after the color-switching cycle test deserve further investigation. $\text{Rb-TiO}_2/\text{TB-CS}$ from DEG-added nanodispersion exhibits no apparent change in the morphology and grain structure after 50 color-switching cycles (Figure S17, Supporting Information). It cannot be ignored that although the slow electron injection leads to the inhibition of the decomposition of the keto radical $\text{Ti}^{4+}\text{-O}\cdot\text{CH-R}$ to form R-CHO due to the breaking of the strong Ti-O bond, the DEG may decompose after scavenging holes in the color-switching cycles. The analysis based on the XPS spectra of C 1s demonstrates that the partial DEG ligand undergoes decomposition after scavenging holes and new DEG molecules would be liganded to the particle surface (see detailed data and discussion in Figure S18, Supporting Information). Sufficient DEG in the solvent environment ensures a long-term supply of sacrificial electron donors on the particle surface to counteract the decomposition of DEG. The thermogravimetric analysis (TGA) of DEG-ligated $\text{Rb-TiO}_2/\text{TB}$ nanoparticles is performed to determine the surface content of chemisorbed DEG, and the coverage of the DEG before and after 50 color-switching cycles is calculated to be 5.76 and 5.19 nm⁻², respectively (see detailed data and discussion in Figure S19, Supporting Information). Since DEG is added in excess in the system, the decrease in chemisorbed DEG content should be attributed to the depletion of oxygen vacancies. Moreover, a longer test of 150 color-switching cycles is used to verify the long-term reversibility of $\text{Rb-TiO}_2/\text{TB-CS}$ from DEG-added nanodispersion. The $\text{Rb-TiO}_2/\text{TB-CS}$ exhibits relatively stable reversibility in long-term color switching and the optical modulation amplitude at 650 nm gradually stabilizes at \approx 65% over 150 color-switching cycles (Figure S20, Supporting Information). It is still enough to perform a clear photochromic contrast and the dark blue color (high optical modulation amplitude) can be obtained by increasing the UV irradiation time (Figure S21, Supporting Information). In summary, the number of oxygen vacancies determines the long-term stability of the system and can reach a steady state in 150 color-switching cycles, which may be attributed to the synergistic effect of Rb doping and lattice strain on balancing oxygen vacancies.

Due to the variety of environmental conditions in practical applications, it is essential to study the performance and stability of materials under different conditions. The optical modulation amplitude, response time, and color-switching reversibility of DEG-added $\text{Rb-TiO}_2/\text{TB-CS}$ nanodispersion at different temperatures, humidities, and UV light intensities are further studied. The data and details are shown in Figures S22–S24 (Supporting Information), and the following conclusions can be obtained. Temperature has little effect on optical modulation amplitude and color-switching reversibility, but higher temperature significantly accelerates the oxidation of Ti^{3+} , thereby shortening the recovery time (Figure S22, Supporting Information). Humidity only exhibits an effect on color-switching reversibility. With increasing humidity, the color-switching reversibility weakens, which is attributed to the increased dissociative adsorption of H_2O on oxygen vacancies, reducing the hole scavenging ability (Figure S23, Supporting Information). The UV light intensity

only affects the response time during the coloring stage, which decreases as the UV light intensity increases (Figure S24, Supporting Information). Further, the practical applications of DEG-added Rb-TiO₂/TB-CS nanodispersion deserve to be investigated. Considering the high transparency and large optical modulation amplitude, it can be applied to a photochromic window, which is composed of two quartz glasses and nanodispersion sealed in the middle (Figure S25a, Supporting Information). The photochromic window exhibits high transparency in the absence of UV irradiation and shows a dark blue color to serve as an optical shield after being fully irradiated with UV light (Figure S25b,c, Supporting Information). Moreover, the photochromic response of the nanodispersion to sunlight inspires the application potential of this photochromic window for solar heat and sunlight management.^[34] When exposed to sunlight, the photochromic window absorbs the UV light in sunlight and transforms to a tinted state, thereby reducing sunlight and solar heat entering the room. Importantly, the window is able to adjust its sunlight transmittance and heat absorption capacity in response to changes in sunlight intensity. Figure S26 (Supporting Information) shows how the color of this photochromic window changes over time on a sunny day, dynamically adjusting indoor light to provide good sunlight comfort. Especially in summer, the solar heat gain inside the room is reduced by adjusting the transmittance of sunlight, which reduces the cooling energy consumption of the building. Overall, this photochromic window, which is simple in structure, easy to use, and capable of being activated by low-power UV and sunlight, is of practical significance and opens up new avenues for the design of photochromic devices.

2.3. Density Functional Theory (DFT) Calculations

To further reveal the synergistic effect of epitaxial lattice strain and Rb doping on oxygen vacancy formation as well as the adsorption state of DEG on the particle surface, DFT calculations were performed to analyze the evolution of the oxygen vacancy formation energy and the DEG adsorption energy. According to the quasiharmonic approximation, the change in the Gibbs free energy of oxygen vacancy formation (ΔG) has been shown that it can be described as a function of epitaxial strain (η) and temperature (T) as Equation (1):^[35]

$$\Delta G = \Delta E(\eta) + \Delta F(\eta, T) + \frac{1}{2}x\mu_O(T) \quad (1)$$

where ΔE accounts for the zero temperature contribution to the free energy, ΔF represents the thermal contribution to the free energy, and μ_O represents the oxygen chemical potential. Moreover, ΔG has been described as decreasing with increasing epitaxial strain at constant temperature by Chen,^[35b] suggesting that strain is an effective means of increasing oxygen vacancy concentration. Here tensile strain from 0 to 3% was performed along the x, y, and z directions of the crystal, denoted as TiO₂/TB(X), with X representing the strain level. As shown in Figure 4a, the oxygen vacancy formation energy gradually decreases with increasing lattice strain, implying that the lattice strain effectively reduces the energy barrier for the formation of oxygen vacancy. Furthermore, the doping of the low-valent metal ions generates an effective positive charge (hole state) at the anion lattice position,

and oxygen vacancies are spontaneously formed by a charge compensation mechanism, which releases electrons to fill the formed holes, thus maintaining the charge neutrality of the material.^[11] The first main group elements with the lowest positive valence state (+1) are the optimal choice to significantly reduce the oxygen vacancy formation energy through the charge compensation mechanism. Among the common first main group elements (Li, Na, K, and Rb), Rb has a larger ionic radius, which may cause lattice distortions thereby altering the coordination environment to decrease the migration barrier for oxygen atom transfer and surface exchange. It has also been reported that Rb doping exhibits the most significant reduction in oxygen vacancy formation energy compared to Li, Na, and K.^[11] Correspondingly, Rb doping based on a 3% lattice strain further reduces the oxygen vacancy formation energy to a negative value, ensuring the spontaneous formation of oxygen vacancies (Figure 4a). Therefore, lattice strain and Rb doping synergistically and significantly reduce ΔG , which leads to an exponential increase in oxygen vacancy concentration according to Equation (2).

$$C_{\text{TiO}_{2-x}} = \frac{K \cdot C_{\text{TiO}_2}}{C_{\text{O}_2^{\frac{1}{2}x}}} = \frac{C_{\text{TiO}_2}}{C_{\text{O}_2^{\frac{1}{2}x}}} e^{(-\frac{\Delta G}{RT})} \quad (2)$$

where C_A represents the concentration of A, K is the equilibrium constant, and R is the gas constant. The increased oxygen vacancies facilitate the dissociative adsorption of DEG serving as SED to scavenge holes.

Since the adsorption state of DEG on the particle surface is crucial for the hole scavenging rate, the adsorption energies of two physisorbed configurations and one dissociatively adsorbed configuration of DEG on TiO₂ and Rb-TiO₂/TB(3%) were calculated (Figure 4b). For TiO₂, the dissociative adsorption energy of DEG is more positive than the physical adsorption energy, indicating that the intact DEG physical adsorption configuration is more stable. Notably, the dissociative adsorption energy of DEG on Rb-TiO₂/TB(3%) at oxygen vacancy is more negative than the physical adsorption energy, indicating that DEG prefers to be dissociatively adsorbed at oxygen vacancy in Rb-TiO₂/TB(3%). In addition, compared to TiO₂, the physical adsorption and dissociative adsorption energies of DEG on Rb-TiO₂/TB(3%) exhibit a significant decrease, suggesting that both adsorptions are promoted on Rb-TiO₂/TB(3%). This facilitates the rapid scavenging of holes and stabilizes the coloring state by blocking O₂ through the physisorption layer of DEG. Figure 4c shows the density of states of Rb-TiO₂/TB(3%). The O 2p orbitals contribute the most to the top of the valence band (VB), and Ti 3d orbitals contribute the most to the bottom of the conduction band (CB). Possibly due to the presence of only one valence electron and small doping amount, the orbitals of Rb contribute little to CB and VB, without the introduction of intermediate energy levels in the bandgap. After physical or chemical adsorption, the density of states of Rb-TiO₂/TB(3%) shows no noticeable change (Figure S27, Supporting Information), which indicates that the DEG adsorbed on the surface has no detrimental effect on the electronic structure of the crystal. The density of states of DEG before and after adsorption is displayed in Figure 4d. The bonding orbital energies of DEG in two adsorption states are both shifted in the negative direction, indicating the strong interaction between DEG and the surface of

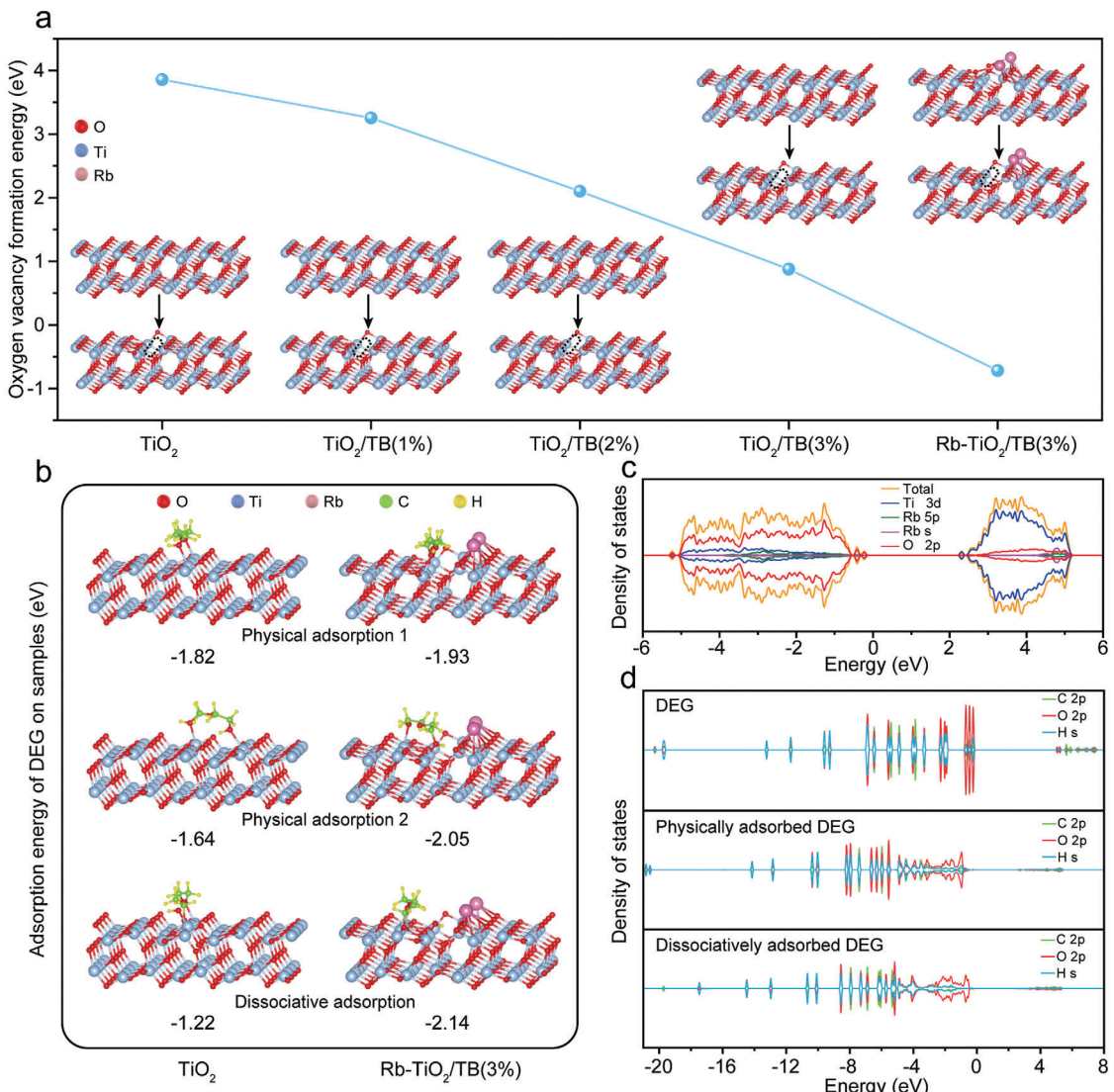


Figure 4. DFT calculations: a) Oxygen vacancy formation energy of TiO_2 , TiO_2/TB with different lattice strain levels (1%, 2%, and 3%), and $\text{Rb-TiO}_2/\text{TB}(3\%)$. b) Adsorption energy of DEG on TiO_2 and $\text{Rb-TiO}_2/\text{TB}(3\%)$. c) Density of states of $\text{Rb-TiO}_2/\text{TB}(3\%)$. d) Density of states of DEG, physically adsorbed DEG, and dissociatively adsorbed DEG on $\text{Rb-TiO}_2/\text{TB}(3\%)$.

Rb-TiO₂/TB(3%).^[36] It is noteworthy that the two adsorption states correspond to different reductions in bonding orbital energy, suggesting that the dissociatively adsorbed surface can better stabilize the DEG, which is consistent with the results of the reduction in adsorption energy. Moreover, compared to physically adsorbed DEG, the O 2p orbital on the left side of the Fermi level of dissociatively adsorbed DEG is shifted toward higher energies, which is mainly contributed by the dissociative hydroxyl oxygens.

Additionally, to verify that it is the chemisorbed DEG that scavenges holes rather than the hydroxyl radicals formed by oxygenation of adsorbed water or solvent, MB was used as the probe molecule to study the mechanism. It is well known that MB can be degraded by oxidative species (such as holes, hydroxyl radicals, etc.) during the photocatalytic process, leading to irreversible discoloration. However, it is important to note that since the reduction potential of MB is lower than that of the photogenerated

electrons of TiO_2 , MB can also be reduced by these electrons to form the colorless *leuco*-methylene blue (LMB).^[37] The colorless LMB can subsequently be oxidized back to the colored MB by O_2 , enabling reversible coloring. Therefore, the color change trend of the MB solution with the addition of Rb-TiO₂/TB-CS after UV irradiation can provide insights into the behavior of holes in the photocatalytic process. As shown in Figure S28 (Supporting Information), the MB solution with Rb-TiO₂/TB-CS completely fades after 120 s under UV irradiation, followed by gradual color recovery in the dark within 24 h. This indicates that MB is reduced to colorless LMB by photogenerated electrons and oxidized back to MB by O_2 in the air, demonstrating effective hole scavenging. However, MB solution containing commercial P25 exhibits minimal color change after 120 s of UV irradiation and completely fades after 70 min of UV irradiation, failing to recover its color in the dark. It can be attributed to the

irreversible degradation by oxidative species generated via holes in MB solution containing commercial P25. Moreover, the DEG's role as a sacrificial electron donor for scavenging holes is further confirmed by fluorescence spectroscopy analysis (Figure S29, Supporting Information). Furthermore, the gas chromatography (GC) analysis is applied to demonstrate the existence of oxidative dissociation products of DEG, referring to the reported analytical approach.^[38] As the data and experiment steps are presented in Figure S30 (Supporting Information), the oxidative dissociation products from DEG are successfully detected, and the percentage of oxidative dissociation products of polyols from solvent environments increases with increasing color-switching cycles. This demonstrates the role of DEG as the sacrificial electron donor to scavenge holes and the substitution of new ligands from the environment.

2.4. Photochromic Composite Materials Constructed with Rb-TiO₂/TB-CS

The above advanced color-switching system was used as the responsive material for transparent photochromic display applications. We designed a polyacrylate-based hybrid material with DEG chemisorbed Rb-TiO₂/TB-CS as the functional component, as illustrated in Figure 5a. Poly(ethylene glycol) diacrylate (PEGDA) and methyl methacrylate (MMA) as monomers and pentaerythritol triacrylate (PETA) as a 3D crosslinker provide the polymer matrix with good strength and flexibility. The DPSi on the Rb-TiO₂/TB-CS surface ensures the monodispersity of the nanoparticles, and APSi which possesses the acrylate structure acts as the site for the hybridization cross-linking reaction, facilitating the construction of a homogeneous and transparent Rb-TiO₂/TB-CS/acrylate photochromic hybrid film by UV curing. The Rb-TiO₂/TB-CS/acrylate hybrid film can be bent extensively and recovered, demonstrating excellent toughness and flexibility (Figure S31, Supporting Information). The scanning electron microscopy (SEM) image and elemental maps of this hybrid film are shown in Figure S32 (Supporting Information), indicating a flat surface and uniform elemental distribution of the hybrid film. It can be seen from Figure 5b that the Rb-TiO₂/TB-CS/acrylate hybrid film shows excellent transparency in the colorless state and exhibits high contrast after UV irradiation. Transparent and colored states can be easily switched by UV irradiation and heat oxidation. In addition, customized contents can be clearly displayed on the hybrid film by UV irradiation using a photomask, which is easily prepared by inkjet printing on a transparent plastic sheet. As shown in Figure 5c, the exposed areas of the photomask turn dark blue after light printing, while the unexposed areas remain transparent, making it easy to light-print complex shapes and text with high resolution. Photo-printed content shows good stability and remains readable after 14 h at room temperature (Figure S33, Supporting Information).

The photochromic response rate of hybrid films with different Rb-TiO₂/TB-CS contents is further investigated. The thickness of the photochromic hybrid films is measured to be 0.8 mm. As seen in Figure 5d, the hybrid films with low Rb-TiO₂/TB-CS content (5 wt.%, 10 wt.%) only exhibit slight coloration after 70 s of UV irradiation. With the increase of Rb-TiO₂/TB-CS content, the coloration process is significantly accelerated. For the

hybrid film with 40 wt.% Rb-TiO₂/TB-CS, the deep dark blue coloration can be accomplished within 30 s of UV irradiation. Additionally, the optical transmittance of the hybrid film in the colorless state is also an important performance index for its application (Figure 5e). The polyacrylate film without Rb-TiO₂/TB-CS exhibits a visible light transmittance greater than 90%, indicating excellent visible transparency. As the Rb-TiO₂/TB-CS content increases, the visible transmittance of the hybrid films gradually decreases, while the UV-shielding ability increases. The decrease in visible transmittance is attributed to the combination of the lone pair electrons of the acrylate with the Lewis acid sites on the TiO₂ surface to form a dipole layer toward the inner TiO₂, which significantly enhances the exciton binding energy, leading to a red-shifting of the absorption band edges.^[39] The hybrid film with 20 wt.% Rb-TiO₂/TB-CS still shows the transmittance of more than 85% at 650 nm and achieves a deep dark blue coloration after 70 s of UV irradiation, so it is chosen for further studies.

The color-switching performance and reversible stability of this hybrid film are also further investigated. As seen in Figure 5f, the transmittance of hybrid film with 20 wt.% Rb-TiO₂/TB-CS gradually decreases with the increasing time of UV irradiation and reaches the minimum in 70 s, exhibiting an optical modulation amplitude of 82.74% at 650 nm, which demonstrates the rapid response and high contrast of this photochromic system. The photochromism performance of the hybrid film under sunlight is also investigated and displayed in Figure S34 (Supporting Information). The transmittance of hybrid film gradually approaches the minimum after 150 min of sunlight irradiation and the optical modulation amplitude is reduced to 60.7% at 650 nm. Nevertheless, the complex patterns and texts can still be photo-printed on hybrid film through a photomask under sunlight exposure (Figure S35, Supporting Information). The deep dark blue hybrid film left in the air at room temperature takes 24 h to fully recover the transparent state. To accelerate the decoloration process, the hybrid film can be heated in air at 70 °C, which reduces the recovery process to 70 min (Figure 5g). The color-switching reversibility was also evaluated by studying the transmittance of hybrid film for coloration and decoloration in 20 repetitive cycles (Figure 5h). The transmittance of the hybrid films shows no noticeable change after successive coloration-decoloration cycles and still exhibits an optical modulation amplitude exceeding 75% after 20 cycles, indicating the stable reversibility of the hybrid films dominated by Rb-TiO₂/TB-CS. Therefore, Rb-TiO₂/TB-CS/acrylate photochromic hybrid film exhibiting large optical modulation amplitude, rapid response, and stable reversibility has the potential to serve as an adaptable base material. For instance, it can be used to construct indoor transparent display devices. Figure S36a (Supporting Information) illustrates the potential application scenario, such as the transparent glass for advertising and displaying contents in conference rooms. Figure S36b (Supporting Information) depicts that the transparent display glass is composed of two quartz glasses and a Rb-TiO₂/TB-CS/acrylate hybrid film sandwiched in between. The transparent display glass exhibits good transparency to clearly present the scene behind the glass (Figure S36c, Supporting Information). The photo-printed contents can be clearly displayed with high contrast on the transparent base (Figure S36d,e, Supporting Information). In addition, photo-printing can be performed directly with a programmable UV laser without the use of a

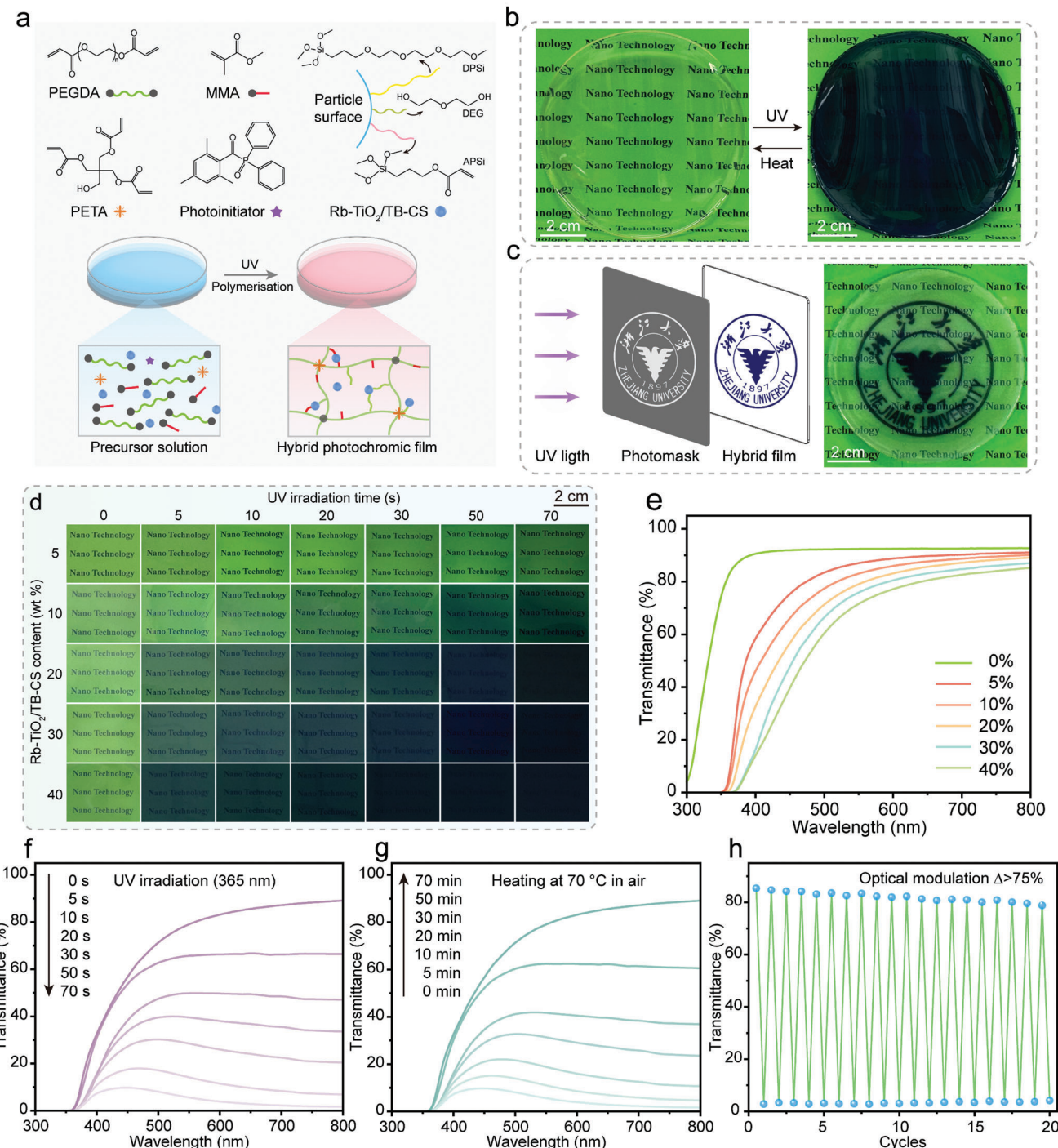


Figure 5. Rb-TiO₂/TB-CS/acrylate photochromic hybrid films: a) Schematic diagram of the composition and preparation process of the hybrid film. b) Reversible color switching of hybrid films. c) Schematic illustration of displaying customized content on the hybrid film through a photomask and an optical image of the hybrid film with a photo-printed logo pattern. d) Photographs of photochromic behavior of hybrid films with different Rb-TiO₂/TB-CS contents as a function of UV irradiation time. e) Optical transmittance of hybrid films with different Rb-TiO₂/TB-CS contents. f) UV-vis transmission spectra of the hybrid film with 20 wt.% Rb-TiO₂/TB-CS during UV irradiation. g) UV-vis transmission spectra of the colored hybrid film with 20 wt.% Rb-TiO₂/TB-CS heating in air at 70 °C. h) The plots of the transmittance at 650 nm of the hybrid film with 20 wt.% Rb-TiO₂/TB-CS in cyclic tests for photochromism and discoloration.

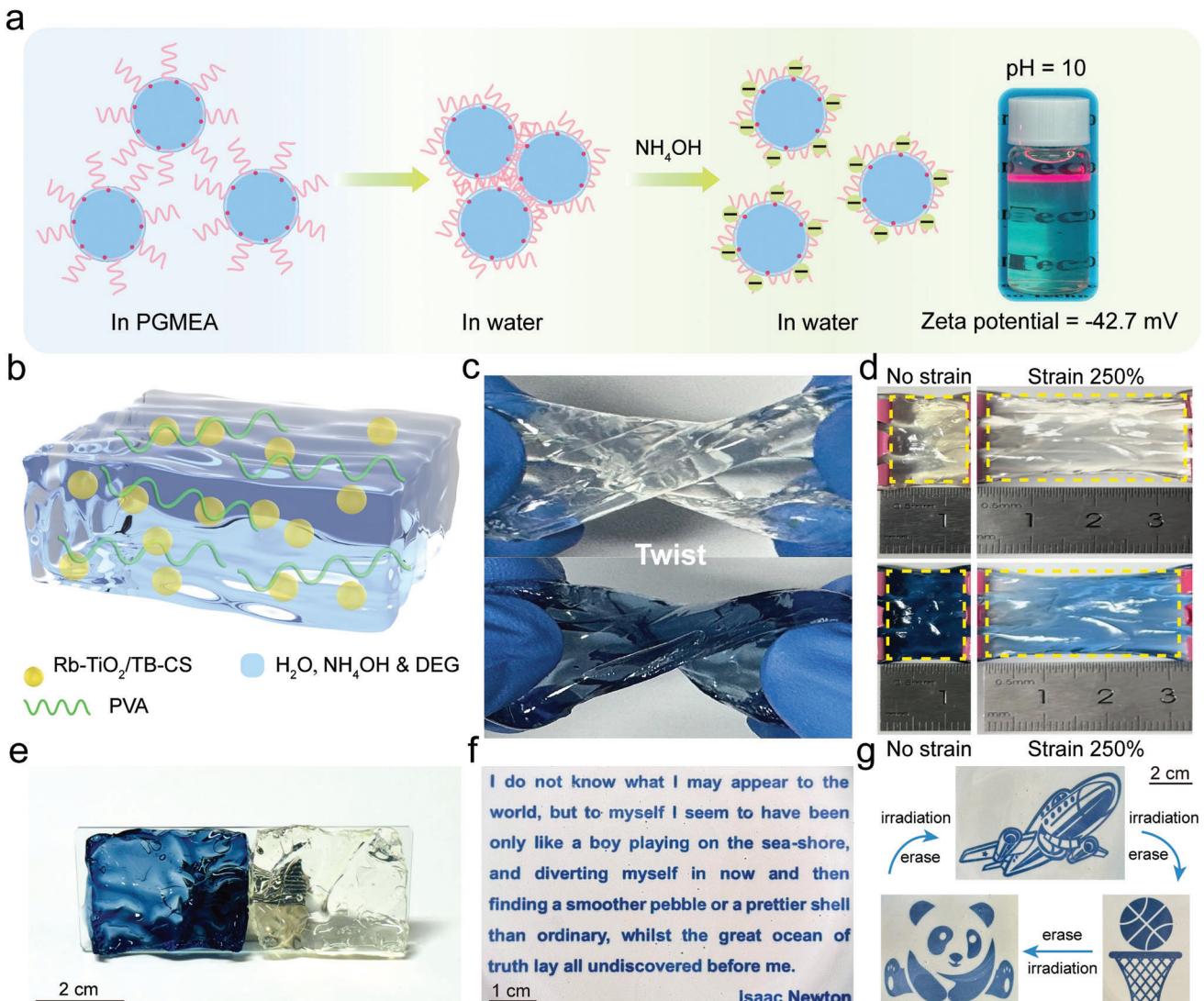


Figure 6. a) Schematic illustration of the dispersion mechanism of Rb-TiO₂/TB-CS in aqueous solution. b) Schematic diagram of the structure of Rb-TiO₂/TB-CS/PVA photochromic hydrogel. c) Twistability, d) stretchability, and e) adhesiveness of the Rb-TiO₂/TB-CS/PVA hydrogel under different color states. Light printing of f) text and g) graphics on Rb-TiO₂/TB-CS/HEC composite rewritable films.

photomask. The utilization of Rb-TiO₂/TB-CS/acrylate hybrid film to construct the transparent display device is simple and feasible, representing a low-cost and advanced solution for transparent displays.

Moreover, Rb-TiO₂/TB-CS also exhibits surprising application potential in aqueous substrates, showing good transparency and photochromic properties. As shown in **Figure 6a**, surface-grafted long-chain siloxane (DPSi) can adjust the surface properties to accommodate organic solvents and acrylate systems. However, in the aqueous solution, the modifiers may rotate and adhere to the surface without providing steric hindrance.^[40] Correspondingly, by adding ammonia to adjust the DEG-added Rb-TiO₂/TB-CS aqueous solution to a weak base (pH 10), the zeta potential is measured to be -42.7 mV to prove the wide electric double-layer of particles, suggesting that the particles can be monodispersed by mutual repulsion through electrostatic interactions.

As shown in Figure S37 (Supporting Information), after 90 days of storage the aqueous nanodispersion (10 wt.%) still exhibits no precipitation and maintains excellent transparency. Considering the transparency maintained by electrostatic interactions in aqueous-based conditions, the hydrogel containing Rb-TiO₂/TB-CS is suitable for further applications. As schematically shown in Figure 6b, PVA serves as the hydrogel matrix with water and ammonia to ensure the monodispersion of particles by electrostatic repulsion. The DEG chemisorbed on the particle surface not only acts as the SED to scavenge holes but also enhances the mechanical properties of the hydrogel through hydrogen bonds with the PVA matrix.^[41] Notably, the transparent Rb-TiO₂/TB-CS/PVA hydrogel can be significantly twisted and stretched (250%) in different color states (Figure 6c,d), demonstrating good mechanical properties. Furthermore, the hydrogel can be easily adhered to the material surface (Figure 6e), showing flexibility and

convenience in application, which reveals its potential in applications such as oxygen indicators and wearable devices. Additionally, the construction of photochromic rewritable paper is another attractive application well-suited for Rb-TiO₂/TB-CS. By pouring and evaporating a mixed aqueous solution of Rb-TiO₂/TB-CS, DEG, and HEC on cardboard, Rb-TiO₂/TB-CS/HEC composite film was obtained for photochromic reversible writing. It can be seen clearly from Figure 6f that the high-resolution text in 10-point font size can be easily photo-printed through a photomask, which exhibits excellent readability. Complex and delicate patterns can also be printed (UV light) and erased (heat) reversibly as shown in Figure 6g, and photo-printed content can remain visible for up to 6 h in room condition (Figure S38, Supporting Information). Therefore, Rb-TiO₂/TB-CS/HEC composite film can be used as reversible printing paper for short-term reading, such as temporary labels and confidential documents in conferences.

3. Conclusion

In conclusion, a highly efficient and stable Rb-TiO₂/TB-CS structure is designed for constructing reversible photochromic systems. The oxygen vacancies engineering drastically enhances the photochromic performance of TiO₂. Structural analyses and DFT calculations indicate that Rb doping and tensile strain synergistically promote the generation of oxygen vacancies and facilitate the DEG adsorption on the TiO₂ surface. Chemisorbed DEG acts as the efficient SED to rapidly scavenge holes, and physisorbed DEG may block O₂ to stabilize the coloring state. The engineered DEG-added Rb-TiO₂/TB-CS nanodispersion shows a significant optical modulation amplitude exceeding 90% at 650 nm, rapid response within 60 s, and stable reversibility, which can be used to construct photochromic windows. Additionally, the Rb-TiO₂/TB-CS nanoparticles are modified using composite siloxanes to be monodispersed with an average size of 11.7 nm and improve the organic-inorganic compatibility, which enables the high transparency of photochromic composite materials. The transparent Rb-TiO₂/TB-CS/acrylate photochromic hybrid film possesses good flexibility and shows an optical contrast of 82.74% at 650 nm before and after UV irradiation, which enables photo-printing of complex contents, showing great potential for transparent display applications. The Rb-TiO₂/TB-CS/PVA photochromic hydrogel shows great transparency, stretchability, twistability, and adhesiveness, indicating the application potential in wearable devices. In addition, the Rb-TiO₂/TB-CS/HEC rewritable films can be used as reversible printing paper for short-term reading. Therefore, the Rb-TiO₂/TB-CS structure, which is compatible, low-cost, stable, and nontoxic, is an excellent versatile responsive material for photochromic systems and opens up new opportunities in various color-switching applications.

4. Experimental Section

Materials: Benzyl alcohol (BnOH, ≥99%), titanium butoxide (TBOT, ≥99%), rubidium nitrate (RbNO₃, ≥99%), 3-(acryloyloxy)propyltrimethoxysilane (APSi, ≥99%), 3,3-dimethoxy-2,7,10,13,16-penta-oxa-3-silaheptadecane (DPSi, ≥97%), methylene blue (MB, AR), propylene glycol monomethyl ether acetate (PGMEA, ≥99.5%), diethylene glycol (DEG, ≥99%), poly(ethylene glycol) diacrylate (PEGDA,

Mw ≈ 575), polyvinyl alcohol (PVA, Mw ≈ 195000), and hydroxyethyl cellulose (HEC, 250–450 mPa·s) were provided by Shanghai Macklin Biochemical Co., Ltd. Methyl methacrylate (MMA, ≥99%), pentaerythritol triacrylate (PETA, ≥96%), and diphenyl(2,4,6-trimethylbenzoyl)phosphine oxide (TPO, ≥97%) were obtained from Shanghai Aladdin Biochemical Technology Co., Ltd. Acetic acid (HAc, ≥99.5%), ethanol (EtOH, ≥99.7%), n-heptane (C₇H₁₆, ≥98.5%), ammonium hydroxide (NH₃·H₂O, 28%) and acetone (DMK, AR) were obtained from Sinopharm Chemical Reagent Co., Ltd.

Synthesis of Rb-TiO₂/TB Nanoparticles: Typically, 0.2 mL of HAc, 0.8 mL of H₂O, 0.18 g of RbNO₃, and 6 mL of TBOT were sequentially dissolved in 25 mL of BnOH under stirring. The above precursor solution was transferred to a Teflon-lined autoclave and heated at 200 °C for 2 h. Then the 1.2 mL of TBOT and 30 μL of H₂O were successively added to the above reaction system under stirring, and the mixture solution was sealed and heated at 300 °C for 1 h. The products were separated by centrifugation and washed with PGMEA 3 times. The precipitate was heated at 80 °C for 12 h to obtain the dry powder noted as Rb-TiO₂/TB. Additionally, the pure TiO₂ was prepared without the secondary addition of TBOT and H₂O, and the TiO₂/TB was prepared without the addition of RbNO₃.

Preparation of Rb-TiO₂/TB-CS Nanoparticles and Nanodispersions: The 1.5 g of undried Rb-TiO₂/TB precipitate and 0.25 g of DPSi were added to 10 mL of PGMEA at 130 °C with stirring for 50 min, and then 0.05 g of APSi was added to the mixture with stirring for another 10 min to form a transparent dispersion. The dispersion was precipitated by adding n-heptane as anti-solvent and after centrifugation the precipitate was re-dispersed in acetone. After repeating the backwashing operation 3 times, the precipitate was placed under a vacuum for 2 h to obtain the dry powder noted as Rb-TiO₂/TB-CS. The 1 g of Rb-TiO₂/TB-CS powder was added to 8 mL of PGMEA and 2 mL DEG under stirring to form the transparent Rb-TiO₂/TB-CS photochromic nanodispersion (volume ratio, PGMEA:DEG = 4:1). The 1 g of Rb-TiO₂/TB-CS powder, and 0.5 mL of NH₃·H₂O were added to 10 mL of H₂O under stirring to form the transparent Rb-TiO₂/TB-CS aqueous nanodispersion. Additionally, TiO₂-CS and TiO₂/TB-CS nanoparticles and nanodispersions were also prepared in the same way.

Preparation of Rb-TiO₂/TB-CS/Acrylate Photochromic Hybrid Films: The 1 g of Rb-TiO₂/TB-CS powder, 1.5 mL of MMA, 2.5 mL of PEGDA, 0.2 mL of DEG, 0.4 g of PETA, and 35 mg of TPO were added to 10 mL of acetone under stirring to form the homogeneous precursor solution. After evaporating the solvent (acetone) at 80 °C, the transparent Rb-TiO₂/TB-CS/acrylate photochromic hybrid film was obtained by UV curing the mixture in a glass mold.

Preparation of Rb-TiO₂/TB-CS/PVA Photochromic Hydrogels: The aqueous glue was prepared by dissolving 3 g PVA in 30 mL H₂O at 100 °C. The 10 mL of aqueous glue, 5 mL of Rb-TiO₂/TB-CS aqueous nanodispersion, and 0.5 mL of DEG were mixed to form a homogeneous glue, and then the glue was cast onto a glass mold and heated at 60 °C to fabricate a transparent hydrogel.

Preparation of Rb-TiO₂/TB-CS/HEC Rewritable Films: The HEC stock solution was prepared by dissolving 2 g HEC in 30 mL H₂O at 80 °C for 2 h. The 10 mL of Rb-TiO₂/TB-CS aqueous nanodispersion, 2 mL of DEG, and 15 mL of HEC stock solution were mixed and stirred for 1 h before film deposition. The mixture was cast onto a cardboard mold and heated at 70 °C for 12 h to form a composite photochromic film.

Cyclic Tests for Photochromism and Discoloration: The LED device (18 W, λ = 365 nm) was used as the UV light source with a light intensity of 70 mW cm⁻². For the testing of Rb-TiO₂/TB-CS photochromic nanodispersion (volume ratio, PGMEA:DEG = 4:1), the visible light transmittance of the solution was measured after 60 s of UV irradiation, then air was injected into the solution for complete discoloration and the transmittance was measured again. The above operation is counted as one cycle. For the testing of Rb-TiO₂/TB-CS/acrylate hybrid photochromic films, the UV irradiation time was 70 s and the discoloration condition was dark treatment for 24 h.

Electrochemical Measurements: Electrochemical measurements were carried out using a Bio-Logic VSP electrochemical workstation. The O₂-saturated 0.5 M H₂SO₄ was used as the electrolyte. The Hg/Hg₂SO₄ (K₂SO₄ saturated) electrode and the platinum column were used as the

reference electrode and counter electrode, respectively. To prepare the working electrode, 10 mg of nanoparticle powder was added in a mixture of 0.5 mL of H_2O and 0.5 mL of EtOH. After being sonicated for 5 h, 0.5 mL of the suspension was drop-cast onto carbon paper (effective area 1 cm^2) on a heated plate at 80°C . Cyclic voltammetry (CV) measurements were performed in the non-Faraday potential region with various scan rates (20, 50, 100, 150, and 200 mV s^{-1}). All potentials were referenced to the reversible hydrogen electrode (RHE) as follows:

$$E(\text{RHE}) = E(\text{Hg / Hg}_2\text{SO}_4) + 0.059\text{pH} + 0.643 \quad (3)$$

Characterizations: The X-ray diffraction (XRD) patterns were obtained from Bruker D8 Advance diffractometer ($\text{Cu K}\alpha = 1.5406\text{ \AA}$). The transmission electron microscopy (TEM) images were captured with JEOL JEM-F200 equipped with a dual-probe energy-dispersive spectrometer (EDS). The inductively coupled plasma optical emission spectrometry (ICP-OES) measurements were done on Thermo Fisher iCAP PRO. The UV-vis transmittance, absorbance, and diffuse reflectance spectra (DRS) were tested on Agilent Cary 5000. The Fourier transform infrared (FT-IR) spectra were obtained from Thermo Fisher Nicolet iS50. The size distribution of nanodispersions was analyzed with Malvern Zetasizer Nano-ZS. Electron paramagnetic resonance (EPR) measurements were performed on Bruker E500. The X-ray photoelectron spectroscopy (XPS) spectra were acquired from Thermo Scientific K-Alpha. The scanning electron microscopy (SEM) images were acquired from Hitachi SU-8010.

Supporting Information

Supporting Information is available from the Wiley Online Library or from the author.

Acknowledgements

This study was financially supported by the City Science and Technology Research Project of Quzhou (2022K11, 2023K008), the Research Funds of Institute of Zhejiang University-Quzhou (IZQ2021RCZX038, IZQ2022RCZX017), and the Competitive Science and Technology Program of Zhejiang University-Quzhou (IZQ2023KJ1012).

Conflict of Interest

The authors declare no conflict of interest.

Data Availability statement

The data that support the findings of this study are available from the corresponding author upon reasonable request.

Keywords

lattice strain, oxygen vacancies, photochromic composite materials, Rb doping, titanium dioxide

Received: December 1, 2024

Revised: February 6, 2025

Published online: February 21, 2025

[1] a) M. I. Khazi, W. Jeong, J.-M. Kim, *Adv. Mater.* **2018**, *30*, 1705310; b) J. Zhang, Q. Zou, H. Tian, *Adv. Mater.* **2013**, *25*, 378; c) L. Wang, Q. Li, *Chem. Soc. Rev.* **2018**, *47*, 1044.

- [2] a) K. Li, Y. Xiang, X. Wang, J. Li, R. Hu, A. Tong, B. Z. Tang, *J. Am. Chem. Soc.* **2014**, *136*, 1643; b) Y. Zhu, Y. Yao, Z. Chen, Z. Zhang, P. Zhang, Z. Cheng, Y. Gao, *Sol. Energy Mater. Sol. Cells.* **2022**, *239*, 111664; c) Y. Wu, Y. Xie, Q. Zhang, H. Tian, W. Zhu, A. D. Q. Li, *Angew. Chem., Int. Ed.* **2014**, *53*, 2090; d) L. García-Fernández, C. Herbivo, V. S. M. Arranz, D. Warther, L. Donato, A. Specht, A. del Campo, *Adv. Mater.* **2014**, *26*, 5012; e) W. Meng, J. Wang, L. Jiang, *Responsive Mater.* **2024**, *2*, 20240001.
- [3] a) S. Fredrich, R. Göstl, M. Herder, L. Grubert, S. Hecht, *Angew. Chem., Int. Ed.* **2016**, *55*, 1208; b) H. Dong, H. Zhu, Q. Meng, X. Gong, W. Hu, *Chem. Soc. Rev.* **2012**, *41*, 1754; c) R. Pardo, M. Zayat, D. Levy, *Chem. Soc. Rev.* **2011**, *40*, 672.
- [4] A. B. A. Kayani, S. Kuriakose, M. Monshipouri, F. A. Khalid, S. Walia, S. Sriram, M. Bhaskaran, *Small.* **2021**, *17*, 2100621.
- [5] a) W. Wang, L. Liu, J. Feng, Y. Yin, *Small Methods.* **2018**, *2*, 1700273; b) X. Tian, X. Cai, Z. Zeng, Y. He, X. Xu, L. Lei, C. Xu, X. Xu, Y. Xu, P. Li, X. Zhang, *Chem. Eng. J.* **2024**, *498*, 155304; c) X. Tian, W. Han, Z. Zeng, Y. He, L. Lei, X. Xu, Y. Xu, P. Li, X. Zhang, *Chem. Eng. J.* **2023**, *477*, 146962.
- [6] a) W. Wang, J. Feng, Y. Ye, F. Lyu, Y. Liu, J. Guo, Y. Yin, *Nano Lett.* **2017**, *17*, 755; b) W. Wang, M. Ye, L. He, Y. Yin, *Nano Lett.* **2014**, *14*, 1681; c) W. Wang, N. Xie, L. He, Y. Yin, *Nat. Commun.* **2014**, *5*, 5459; d) Y. Zhang, Y. Dou, Z. Ye, W. Xue, F. Liu, M. Yan, W. Wang, Y. Yin, *Small.* **2023**, *20*, 2310962.
- [7] a) Y. Yin, A. P. Alivisatos, *Nature.* **2005**, *437*, 664; b) H. Althues, J. Henle, S. Kaskel, *Chem. Soc. Rev.* **2007**, *36*, 1454.
- [8] W. Meng, A. J. J. Kragt, Y. Gao, E. Bremilla, X. Hu, J. S. van der Burgt, A. P. H. J. Schenning, T. Klein, G. Zhou, E. R. van den Ham, L. Tan, L. Li, J. Wang, L. Jiang, *Adv. Mater.* **2023**, *36*.
- [9] a) D. Han, B. Jiang, J. Feng, Y. Yin, W. Wang, *Angew. Chem., Int. Ed.* **2017**, *129*, 7900; b) W. Wang, Y. Ye, J. Feng, M. Chi, J. Guo, Y. Yin, *Angew. Chem., Int. Ed.* **2015**, *54*, 1321.
- [10] a) S. Yamazaki, H. Ishida, D. Shimizu, K. Adachi, *ACS Appl. Mater. Interfaces.* **2015**, *7*, 26326; b) C. Di Valentini, D. Fittipaldi, *J. Phys. Chem. Lett.* **2013**, *4*, 1901; c) A. T. Smith, H. Ding, A. Gorski, M. Zhang, P. A. Gitman, C. Park, Z. Hao, Y. Jiang, B. L. Williams, S. Zeng, A. Kokkula, Q. Yu, G. Ding, H. Zeng, L. Sun, *Matter.* **2020**, *2*, 680; d) S. Yamazaki, D. Shimizu, S. Tani, K. Honda, M. Sumimoto, K. Komaguchi, *ACS Appl. Mater. Interfaces.* **2018**, *10*, 19889.
- [11] J. J. Carey, M. Nolan, *J. Mater. Chem. A.* **2017**, *5*, 15613.
- [12] C. Balaji Gopal, M. García-Melchor, S. C. Lee, Y. Shi, A. Shavorskiy, M. Monti, Z. Guan, R. Sinclair, H. Bluhm, A. Vojvodic, W. C. Chueh, *Nat. Commun.* **2017**, *8*, 15360.
- [13] U. Aschauer, R. Pfenninger, S. M. Selbach, T. Grande, N. A. Spaldin, *Phys. Rev. B.* **2013**, *88*, 054111.
- [14] a) X. Liu, L. Zhang, Y. Zheng, Z. Guo, Y. Zhu, H. Chen, F. Li, P. Liu, B. Yu, X. Wang, J. Liu, Y. Chen, M. Liu, *Adv. Sci.* **2019**, *6*, 1801898; b) M. Kubicek, Z. Cai, W. Ma, B. Yıldız, H. Hutter, J. Fleig, *ACS Nano.* **2013**, *7*, 3276; c) J. R. Petrie, H. Jeen, S. C. Barron, T. L. Meyer, H. N. Lee, *J. Am. Chem. Soc.* **2016**, *138*, 7252; d) J. R. Petrie, C. Mitra, H. Jeen, W. S. Choi, T. L. Meyer, F. A. Reboredo, J. W. Freeland, G. Eres, H. N. Lee, *Adv. Funct. Mater.* **2016**, *26*, 1564.
- [15] Y. Liu, X. Wang, X. Li, Z. Ye, T.-K. Sham, P. Xu, M. Cao, Q. Zhang, Y. Yin, J. Chen, *Nat. Commun.* **2024**, *15*, 9357.
- [16] a) C. Adán, A. Bahamonde, M. Fernández-García, A. Martínez-Arias, *Appl. Catal. B.* **2007**, *72*, 11; b) K. Wilke, H. D. Breuer, *J. Photochem. Photobiol. A.* **1999**, *121*, 49.
- [17] a) S. Liang, X. Wang, R. Qi, Y.-J. Cheng, Y. Xia, P. Müller-Buschbaum, X. Hu, *Adv. Funct. Mater.* **2022**, *32*, 2201675; b) J. Zhao, B. Chen, F. Wang, *Adv. Mater.* **2020**, *32*, 2004142.
- [18] a) S. Zhou, H. Jang, Q. Qin, L. Hou, M. G. Kim, S. Liu, X. Liu, J. Cho, *Angew. Chem., Int. Ed.* **2022**, *61*, 202212196; b) L. Yang, C. Wang, Y. Li, W. Ge, L. Tang, J. Shen, Y. Zhu, C. Li, *Adv. Funct. Mater.* **2024**, *34*, 2401094.

- [19] M. J. Hjorth, E. Snoeck, R. Kilaas, *Ultramicroscopy*. **1998**, *74*, 131.
- [20] S. Cui, J. Wang, H. Xie, Y. Zhao, Z. Li, S. Luo, L. Ke, Y. Gao, K. Meng, L. Ding, Y. Yuan, *Adv. Sci.* **2020**, *7*, 2002445.
- [21] T. Ji, Q. Liu, R. Zou, Y. Sun, K. Xu, L. Sang, M. Liao, Y. Koide, L. Yu, J. Hu, *Adv. Funct. Mater.* **2016**, *26*, 1400.
- [22] A. Sinhamahapatra, J.-P. Jeon, J.-S. Yu, *Energy Environ. Sci.* **2015**, *8*, 3539.
- [23] Y. Zhang, Z. Ding, C. W. Foster, C. E. Banks, X. Qiu, X. Ji, *Adv. Funct. Mater.* **2017**, *27*, 1700856.
- [24] M.-C. Tsai, T.-T. Nguyen, N. G. Akalework, C.-J. Pan, J. Rick, Y.-F. Liao, W.-N. Su, B.-J. Hwang, *ACS Catal.* **2016**, *6*, 6551.
- [25] a) A. Naldoni, M. Allieta, S. Santangelo, M. Marelli, F. Fabbri, S. Cappelli, C. L. Bianchi, R. Psaro, V. Dal Santo, *J. Am. Chem. Soc.* **2012**, *134*, 7600; b) Q. Wu, Q. Zheng, R. van de Krol, *J. Phys. Chem. C* **2012**, *116*, 7219; c) L. Hou, M. Zhang, Z. Guan, Q. Li, J. Yang, *Appl. Surf. Sci.* **2018**, *428*, 640.
- [26] a) R. Jia, Y. Wang, C. Wang, Y. Ling, Y. Yu, B. Zhang, *ACS Catal.* **2020**, *10*, 3533; b) S. Zhang, W. Li, Z. Jin, J. Yang, J. Zhang, Z. Du, Z. Zhang, *J. Solid State Chem.* **2004**, *177*, 1365.
- [27] a) Y. Zhang, N. Cao, H. Cheng, X. Zhao, L. Qiu, Y. Fang, J. Liao, X. Cai, X. Tian, L. Lei, P. Xie, X. Zhang, *Appl. Catal. B* **2024**, *355*, 124171; b) G. Zhu, W. Zhu, Y. Lou, J. Ma, W. Yao, R. Zong, Y. Zhu, *Nat. Commun.* **2021**, *12*, 4152; c) T. R. Gordon, M. Cargnello, T. Paik, F. Mangolini, R. T. Weber, P. Fornasiero, C. B. Murray, *J. Am. Chem. Soc.* **2012**, *134*, 6751.
- [28] a) E. Farfan-Arribas, R. J. Madix, *J. Phys. Chem. B* **2002**, *106*, 10680; b) T. Tachikawa, Y. Takai, S. Tojo, M. Fujitsuka, H. Irie, K. Hashimoto, T. Majima, *J. Phys. Chem. B* **2006**, *110*, 13158.
- [29] a) U. Joost, A. Šutka, M. Oja, K. Smits, N. Döbelin, A. Loot, M. Järvekülg, M. Hirsimäki, M. Valden, E. Nõmmiste, *Chem. Mater.* **2018**, *30*, 8968; b) C. J. Dahlman, A. Agrawal, C. M. Staller, J. Adair, D. J. Milliron, *Chem. Mater.* **2019**, *31*, 502.
- [30] a) B. Wen, Q. Hao, W.-J. Yin, L. Zhang, Z. Wang, T. Wang, C. Zhou, A. Selloni, X. Yang, L.-M. Liu, *Phys. Chem. Chem. Phys.* **2018**, *20*, 17658; b) Z. Wang, B. Wen, Q. Hao, L.-M. Liu, C. Zhou, X. Mao, X. Lang, W.-J. Yin, D. Dai, A. Selloni, X. Yang, *J. Am. Chem. Soc.* **2015**, *137*, 9146.
- [31] O. I. Micic, Y. Zhang, K. R. Cromack, A. D. Trifunac, M. C. Thurnauer, *J. Phys. Chem.* **1993**, *97*, 7277.
- [32] a) I. A. Shkrob, M. C. Sauer, D. Gosztola, *J. Phys. Chem. B* **2004**, *108*, 12512; b) M.-H. Du, J. Feng, S. B. Zhang, *Phys. Rev. Lett.* **2007**, *98*, 066102.
- [33] a) E. Lira, S. Wendt, P. Huo, J. Ø. Hansen, R. Streber, S. Porsgaard, Y. Wei, R. Bechstein, E. Lægsgaard, F. Besenbacher, *J. Am. Chem. Soc.* **2011**, *133*, 6529; b) O. Bikondoa, C. L. Pang, R. Ithnin, C. A. Muryn, H. Onishi, G. Thornton, *Nat. Mater.* **2006**, *5*, 189; c) S. Wendt, P. T. Sprunger, E. Lira, G. K. H. Madsen, Z. Li, J. Ø. Hansen, J. Matthiesen, A. Blekinge-Rasmussen, E. Lægsgaard, B. Hammer, F. Besenbacher, *Science* **2008**, *320*, 1755.
- [34] W. Meng, A. J. J. Kragt, X. Hu, J. S. van der Burgt, A. P. H. J. Schenning, Y. Yue, G. Zhou, L. Li, P. Wei, W. Zhao, Y. Li, J. Wang, L. Jiang, *Adv. Funct. Mater.* **2024**, *34*, 2402494.
- [35] a) S. Baroni, P. Giannozzi, E. Isaev, *Rev. Mineral. Geochem.* **2010**, *71*, 39; b) W. Zhang, L. Cai, S. Cao, L. Qiao, Y. Zeng, Z. Zhu, Z. Lv, H. Xia, L. Zhong, H. Zhang, X. Ge, J. Wei, S. Xi, Y. Du, S. Li, X. Chen, *Adv. Mater.* **2019**, *31*, 1906156.
- [36] S. Hou, D. Fang, Q. Jin, Y. Ye, Q. Li, F. He, J. Xie, *Appl. Surf. Sci.* **2022**, *605*, 154645.
- [37] A. Mills, J. Wang, *J. Photochem. Photobiol. A* **1999**, *127*, 123.
- [38] Y. Liu, C. Zhang, J. Feng, X. Wang, Z. Ding, L. He, Q. Zhang, J. Chen, Y. Yin, *Angew. Chem., Int. Ed.* **2023**, *62*.
- [39] N. Nakayama, T. Hayashi, *Colloids Surf. A* **2008**, *317*, 543.
- [40] Y. Liu, N. Peng, Y. Yao, X. Zhang, X. Peng, L. Zhao, J. Wang, L. Peng, Z. Wang, K. Mochizuki, M. Yue, S. Yang, *Nat. Commun.* **2022**, *13*, 3581.
- [41] P. Liu, B. Wang, C. Wang, L. Ma, W. Zhang, E. Hopmann, L. Liu, A. Y. Elezzabi, H. Li, *Adv. Funct. Mater.* **2024**, *34*, 2400760.